

The discovery, abundances and $[\text{Fe}/\text{H}]_{\text{NB392}}$ distributions of metal-poor stars in the halo of the Milky Way^{*}

Andrew Jenkins¹†, Florence Wragg¹, Joshua Butterworth¹, James Edwards¹
 Claire O’Neill¹, Joe Gough¹ & David Sobral¹‡

¹ Department of Physics, Lancaster University, Lancaster, LA1 4YB, UK

Accepted 30 May 2019. Received 29 May 2019; in original form 25 March 2019

ABSTRACT

By boldly looking where no one has looked before, this study surveyed a volume within the Milky Way halo to discover population III stars or their direct descendants. A catalogue of 123,505 sources was obtained by surveying the COSMOS field with the WFC and the NB392 filter ($\lambda_c=3918\text{\AA}$, $\Delta\lambda=52\text{\AA}$), sensitive to CaHK. A star-galaxy cut was devised from samples of confirmed stars and galaxies based on spectroscopic redshifts and the apparent optical and infra-red colours of the samples, with a completeness and contamination of 75.3% and 6.1% respectively. The catalogue was reduced to 338 potential stars by introducing a limiting magnitude of 24.7, making it 5-7 magnitudes deeper than the Pristine survey and corresponding to a limiting distance of 166 kpc for G-type stars. This survey covered 1.89 deg^2 , corresponding to volumes from $(1.89 \times 10^8)\text{pc}^3$ to $(8.55 \times 10^{16})\text{pc}^3$ from spectral types M to O. Stars with known metallicity, $[\text{Fe}/\text{H}]$, values from the POLLUX database were used to create an $[\text{Fe}/\text{H}]_{\text{NB392}-u} - (g-i)$ by $(g-i)$ grid and the 338 candidates were assigned metallicity values. This created a final catalogue that was sorted by metallicity and candidates with $[\text{Fe}/\text{H}] < -3$ were visually inspected using the *HST* F814W filter to determine whether they were stars, in which seven were found. These could give an insight to the earliest stars in the universe. Number densities were calculated for F, G and K-type stars with $[\text{Fe}/\text{H}]$ values of -4 to be $(4.3 \pm 3.0) \times 10^{-14} \text{ pc}^{-3}$, $(1.36 \pm 0.96) \times 10^{-13} \text{ pc}^{-3}$ and $(3.0 \pm 2.1) \times 10^{-11} \text{ pc}^{-3}$ respectively. It was found that the number density of stars with $[\text{Fe}/\text{H}] < -3$ is less than expected by a factor of ~ 10.8 , however it is ≈ 6.3 times larger for stars with $[\text{Fe}/\text{H}] < -4$.

Key words: Milky Way halo, Metal-poor, Population III, NB392, CaHK, Python.

1 INTRODUCTION

In 1944, Walter Baade categorised groups of stars within the Milky Way into stellar populations I and II (Gray & Corbally 2009). Population I (Pop I) stars are characterised as blue, very metal-rich, and some of the youngest stars in the Universe. These stars form in the remnants of countless supernovae, in active star forming regions and open star clusters, accompanied by gas and dust. Due to their relatively recent creation, many Pop I stars will still be on the main sequence branch of their lifetime, regardless of their spectral type. Population II (Pop II) stars are characterised as red,

metal-poor stars that are old, and formed before their Pop I predecessors. These stars form in the remnants of metal produced by earlier stars and are mainly found in globular clusters. More massive Pop II stars, for example O stars, will have already gone supernova, and B and A spectral types will have already burned all of their fuel and branched off the main sequence, whereas lower mass stars like F, G, K or M will still be on their main sequence. In the structure of the Milky Way, Pop I stars are mainly found in the disk and the bulge, while Pop II are mainly found in the halo and the bulge.

Both Population I and II stars, however, are successors of the first generation of stars, Population III, which is a category that was later added by astronomers. Population III (Pop III) stars were created in the first Gyr of the Universe (Caffau et al. 2017) where there were no elements heavier than hydrogen and helium, making them the most metal-poor stars in the Universe. The CNO chain be-

^{*} Based on the COSMOS *HST* Survey as well as observations obtained by the Isaac Newton Telescope (INT), programs: I13AN002, I14AN002, 088-INT7/14A, I14BN006, I18-INT13/14B & I15AN008.

† E-mail: a.t.jenkins@lancaster.ac.uk

‡ PHYS369 supervisor.

comes dominant in Pop I and II at high mass, and limits the size of the most massive stars, however the lack of carbon, nitrogen and oxygen meant that the CNO process was not possible and the PP chain remained the dominant form of fusion. This means that Pop III stars would be able to have masses of up to $M_* \approx 1000M_\odot$ (Hosokawa et al. 2016) and would be extremely blue. The super-massive nature of these stars, however, means that the lifetimes of Pop III stars can be extremely short, possibly as short as 1Myr (Chon & Latif 2017). If there are Pop III stars remaining in the Milky Way, they will be in the galactic halo, as this region has a higher concentration of globular clusters and field stars, and is located away from the star-forming regions of the galactic bulge and disk.

Pop III stars are thought to be partly responsible for the re-ionisation of the Universe as they emit high energy LyC radiation. This radiation created areas of ionised hydrogen that would later be able to form stars, and therefore galaxies, allowing Pop III supernovae to create the first metals. The commonplace, high-mass Pop III stars which would be easily seen would have expended their fuel and undergone supernova long ago, however lower-mass stars such as G or K-type stars may still be present in our galaxy.

No confirmed Pop III stars have been found so far. As the massive size links to a short lifetime, Pop III stars are still currently a theoretical category though the evidence that they must have existed at some point is overwhelming. Within this search, the objective is to discover stars with metallicities, which is defined as the proportion of material in a star that is not hydrogen or helium, lower than -6 . At these metallicities, this means a star could potentially be of the first generations of stars, which would put it in the classification of mega metal-poor stars (MMP); (Beers & Christlieb 2005). Previous searches for metal-poor stars include the Pristine survey which have recently found an ultra metal-poor star in the galactic halo with $[\text{Fe}/\text{H}] = -4.66 \pm 0.13$ (Starkenburg et al. 2018) and an apparent $[\text{Fe}/\text{H}] < -7$ star has also been observed (Keller et al. 2014). There are also suggestions that the redshift $z = 6.6$ galaxy COSMOS Redshift 7 (CR7); (Sobral et al. 2015) may contain a $10^7 M_\odot$ Pop III stellar cluster as it has no detected metal emission lines (Lee et al. 2016).

Population III stars represent the key to understanding the history of the Universe, and provide a unique opportunity to look back into the unknown and gain knowledge of the past. WARP are somewhat hopeful that this study may be able to find these early stars in the furthest and oldest regions of our galaxy as it is the first to look at this area of the galactic halo with the intention of finding metal-poor stars. This project will work with both theoretical predictions and data from the Isaac Newton Telescope to try and determine the metallicities of stars in a small volume of the galactic halo, and use this to find the number density of each spectral type at different metallicity brackets. The lowest metallicity results, $[\text{Fe}/\text{H}] < -3.5$, will then be investigated individually to remove any anomalous candidates such as galaxies.

2 CATALOGUE AND DATA

The catalogue of data used in this study was obtained using the 2.54m Isaac Newton Telescope on La Palma. The INT



Figure 1. An image of the observatory housing the Isaac Newton Telescope which was used as the source for the catalogue of data used in this study.

Filter name	λ (Å)	λ_{eff} (Å)	FWHM (Å)
NB392	3786 – 4094	3917	53.63
<i>u</i>	3020 – 4540	3823	528.7
<i>g</i>	3790 – 5667	4780	1155
<i>i</i>	6720 – 9170	7641	1395

Table 1. The various filters that were used during this investigation, with their corresponding range of wavelengths, effective wavelength and full-width half-maximum. The values were obtained through the application of PYTHON scripts onto the filter profiles.

was originally based in England in the 1960s. It was then decided that the telescope should be moved to its better current location; the Canary Islands. The move was completed in 1984 and the INT began working from the Roque de los Muchachos, the highest point on the island.

This study uses images from the Wide Field Camera which consists of four EEV 2kx4k CCDs to create a 33 arcminute field of view. The data was recorded with the NB392 (created by Sobral et al. 2017) ($\lambda_c = 3918 \text{ \AA}$, $\Delta\lambda = 52 \text{ \AA}$) in the narrow-band as well as several broad-band filters. The data used in this survey was produced using the INT/WFC (Sobral et al. 2017) over the course of two years of observations, from 2013 to 2015, and the data reduction of the initial NB392 observations was performed in PYTHON using the methods presented in Stroe et al. (2014) and Stroe & Sobral (2015).

During this investigation, the number of sources was heavily reduced using a variety of methods to eliminate galaxies and sources with extreme values, discussed in Section 3.1. With these methods, there was still always a chance, due to contamination, that the source was not a star and so to verify that the final candidates were stars, the *HST*'s COSMOS survey was used (Scoville et al. 2007).

The COSMOS Survey is aimed at studying galaxies but the images taken within its 2 deg^2 FOV encompass the data used in this study so a visual check could be performed on the final catalogue. For stars of low metallicity, with shallow absorption lines easily lost to noise, iron abundance can be

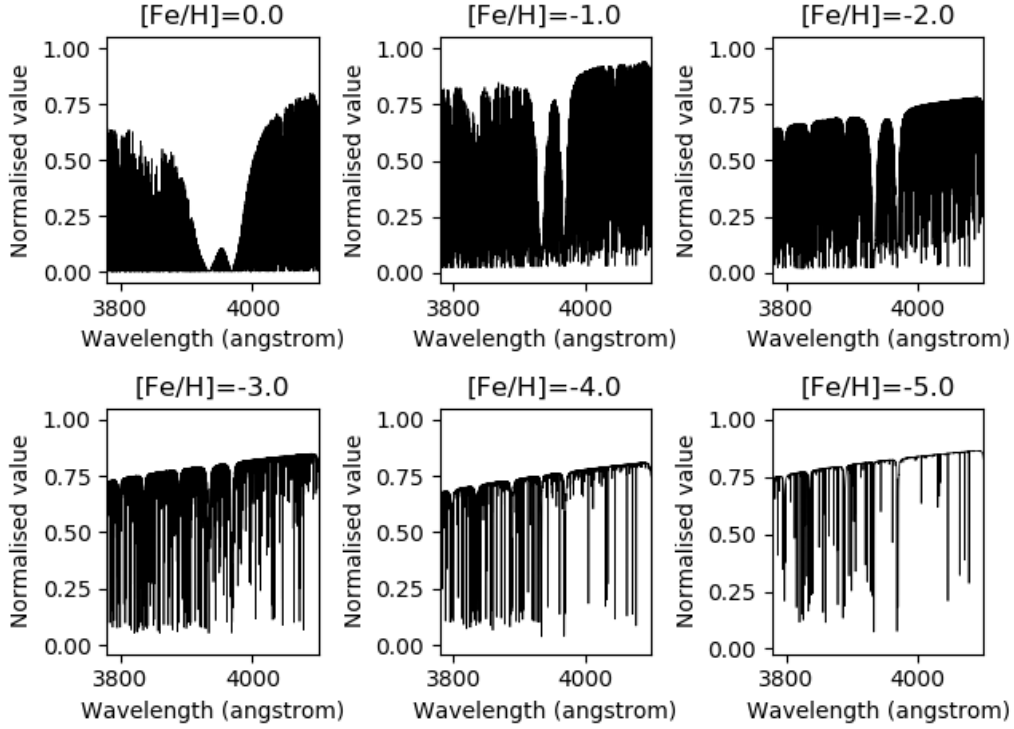


Figure 2. A demonstration of the variation in CaHK absorption within a G-type star’s spectra with changes in metallicity, $[\text{Fe}/\text{H}]$. The relative absorption can be seen to diminish as $[\text{Fe}/\text{H}]$ values decrease which is evidently due to the inherent reduction of Fe and Ca abundance in stars that are more metal-poor.

difficult to measure, however other elements may be used to give an equivalent value of iron abundance.

The CaHK absorption lines, located at 3969.59\AA and 3934.78\AA respectively (Zhu & Ménard 2013) have a more pronounced shape for greater sensitivity to Ca abundance compared to that of Fe and its absorption lines, shown in Figure 2. This makes calcium a good candidate for use in metallicity calculations while ultimately having little effect on the results as iron and calcium are created in very similar fusion processes.

In this investigation, the filters g , i , u and NB392 were chosen. NB392 covers the area of the spectrum containing the characteristic CaHK absorption lines, which are a good measure of $[\text{Fe}/\text{H}]$. For the y -axis in many of the colour-colour graphs $(\text{NB392} - u) - (g - i)$ was used. NB392- u created the best spread of the data points, allowing them to be more easily analysed. By then taking away $(g - i)$, which was also the x -axis, the x dependence of the y -axis was removed, which set the data flat against the x -axis.

In similar studies conducted to measure $[\text{Fe}/\text{H}]$, $\delta(B-V)$ methods are commonly used (Johnson & Morgan 1953). These filters were considered for this study but ultimately $g - i$ was chosen as the separation between the peak wavelengths of the g and i filters provides a good basis for the colour-colour graphs that allow for estimation of temperature and stellar type, shown in Table 2.

Spectral class	Temperature (K)	$g - i$
O	>30000	< -2.60
B	11000 - 30000	-1.32 to -2.60
A	7500 - 11000	-0.227 to -1.32
F	6000 - 7500	0.296 to -0.227
G	5200 - 6000	0.666 to 0.296
K	3500 - 5200	2.96 to 0.666
M	<3500	>2.96

Table 2. A table of spectral classes with their corresponding temperature ranges and $g - i$ values. The method used to determine the $g - i$ values was only accurate for stars with $(g - i) > -0.4$, which encompasses the spread of final star candidates, but is inaccurate at the temperatures of O and B stars due to the extrapolation used.

3 METHODOLOGY

3.1 Catalogue processing

A catalogue of 123,505 sources detected using the NB392 filter was processed to result in a catalogue containing only potential metal-poor stars. The steps taken for reducing this number are shown in Table 3 and discussed more in the following sub-subsections.

3.1.1 Differentiating galaxies from stars

Stars have a redshift of zero, due to sitting within the galactic halo and therefore having no relative movement to the

Step	Description	Condition	Number of remaining sources
0a	NB392 selected for the catalogue	Sourced from Sobral et al. (2017)	123,505
0bi	Obtaining star sample	$z_{spec} = 0$	324 (in sample)
0bii	Obtaining galaxy sample	$0.5 < z_{spec} < 7.0$	2810 (in sample)
1	Creating star-galaxy cut from samples and applying to full catalogue	$U - J > 6.64(J - K) + 2.5$	23,006
2	Removing extreme $U - J$ and $J - K$ values	$(U - J) < 20$ and $-20 < (J - K) < 40$	9,080
3	Limiting errors in $y = (NB392 - u) - (g - i)$ and $x = (g - i)$	$0 < \sigma_y < 0.2$ and $0 < \sigma_x < 0.1$	541
4	Introducing a limiting NB392 magnitude	$NB392 < 24.71$	338

Table 3. The steps taken to reduce the number of sources in the original catalogue to the final group of 338 potential metal-poor stars, further discussed in Section 3.1. The numbers stated for the samples are the number of sources within the sample groups.

Milky Way, and galaxies have a non-zero redshift due to their movement away from the Milky Way. This means that the catalogue could be uploaded to TOPCAT and within the data, a subset could be created of sources that almost certainly were stars by filtering it to only sources with zero redshift. A separate subset was also created of sources that were deemed to be galaxies by filtering it to sources with a redshift between 0.5 and 7.0. Together these subsets created a sample within the data and these were plotted and the axes were changed to different magnitude differences (e.g. $J - K$ against $B - V$) until the most clear separation of stars and galaxies was found. The plot which gave the most defined separation of both groups was $U - J$ against $J - K$ in which a cut was placed at this separation, the line of which is given by Equation 1. Any sources above this line were considered to be stars and any below it were considered to be galaxies. This cut is shown in Figure 3.

$$(U - J) = 6.64(J - K) + 2.5 \quad (1)$$

The cut in the sample was then applied to the whole dataset of 123,505 sources collected with the NB392 filter which reduced it to only sources that were thought to be stars, shown in Figure 4. Creating this star-galaxy cut was the first step in reducing the number of sources in the catalogue and is shown as step 1 in Table 3.

As some values of $U - J$ and $J - K$ had extreme values due to some U , J and K entries having extreme values such as 99, the next step was to eliminate them by limiting their size. The limitations are shown in the condition of step 2 in Table 3.

3.1.2 Estimating completeness and contamination

Completeness is a simple fractional representation of the amount of stars that are encompassed in the sample and was calculated with Equation 2. This equation gave an overall completeness of the sample population of 75.3% which could then be extrapolated as the completeness for the rest of the data.

$$\text{Completeness} = \frac{\text{Recovered stars}}{\text{Total classified stars}} \quad (2)$$

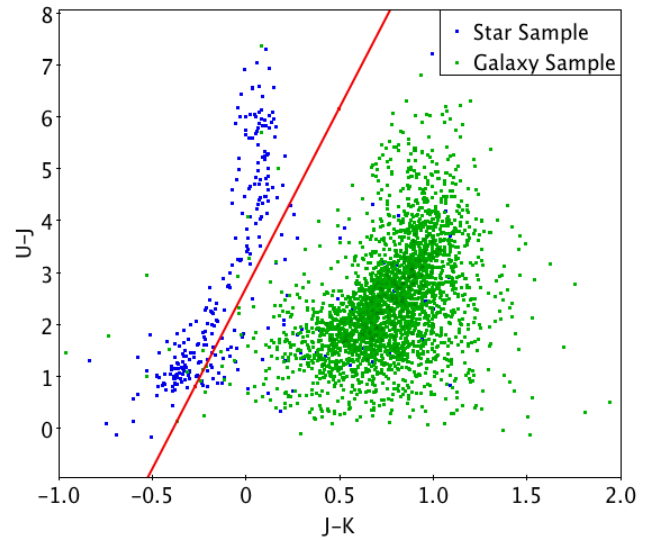


Figure 3. A sample of galaxies and stars, selected from an NB392 filter catalogue of 123,505 sources using spectroscopic redshifts of $z_{spec} = 0$ for stars and $0.5 < z_{spec} < 7.0$ for galaxies, best separated by a cut on a graph of the magnitude differences $U - J$ against $J - K$.

Contamination is a statistical measure of the proportion of the sample star population that have been misidentified. This figure is based on the fraction of objects on the stellar side of the cut which are from the galactic sample group, found using Equation 3. Based on the sample groups used to make the star-galaxy cut, the contamination of the sample population was found to be 6.1%.

$$\text{Contamination} = \frac{\text{Pollutant galaxies}}{\text{Total classified sources}} \quad (3)$$

3.1.3 Errors

To calculate uncertainties for each star's x and y values on Figure 4, their errors in the NB392, u , g and i filter readings

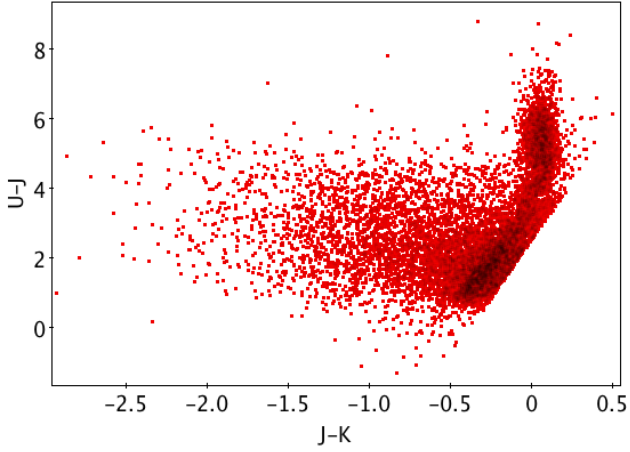


Figure 4. The catalogue of sources after removing the galaxies identified by a star-galaxy cut to the whole dataset.

had to be combined for $g-i$ and $(\text{NB392}-u)-(g-i)$ respectively. Both σ_x and σ_y were found using Equation 4 where A and B are the individual errors of the two elements in the subtraction. This meant the equation had to be performed three times. Once for $A = g$ and $B = i$, again for $A = \text{NB392}$ and $B = u$ then finally for $A = \text{NB392}-u$ and $B = g-i$.

$$\sigma_{(A-B)} = \sqrt{\left(\frac{\delta(A-B)}{\delta A} \Delta A\right)^2 + \left(\frac{\delta(A-B)}{\delta B} \Delta B\right)^2} \quad (4)$$

This equation was used to calculate the error of the data points before being averaged but was found to be far too high; with magnitude errors in x and y in excess of 10.

The y and x errors were used as a limiting factor to further reduce the number of sources, shown as step 3 in Table 3. Histograms were created for the original dataset which are shown in Figures 5 and 6 and any sources with an error of 0.2 in the y -axis and 0.1 in the x -axis were removed and this condition was added to the previously created subset to create a further reduced subset of sources. These values were chosen as it meant that any extreme errors were removed as well as creating a limit in which data above would be increasingly difficult to distinguish star metallicities in Figure 13.

Limiting the σ_x and σ_y to 0.1 and 0.2 respectively was originally done for the purpose of generating a Gaussian distribution of artificial stars to create cuts in various metallicity bands, however this idea was later scrapped in favour of the final method. The limit on σ_x and σ_y , however, was still useful as the final method for calculating metallicity would return a null value if one or both of the errors were too large for the 100x100 grid method used by the code. As a result of these error thresholds, the mean x and y errors were brought from values over 10 down to 0.056765 and 0.106753 respectively.

3.1.4 Limiting magnitude

The last method of catalogue processing was using NB392 magnitudes where, again, a histogram for the whole dataset

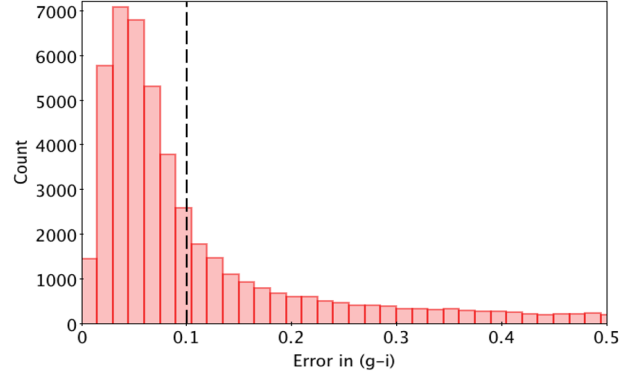


Figure 5. A histogram of the error in the magnitude difference $g-i$ for the whole catalogue. This error was limited to 0.1 so that sources with extreme values could be eliminated.

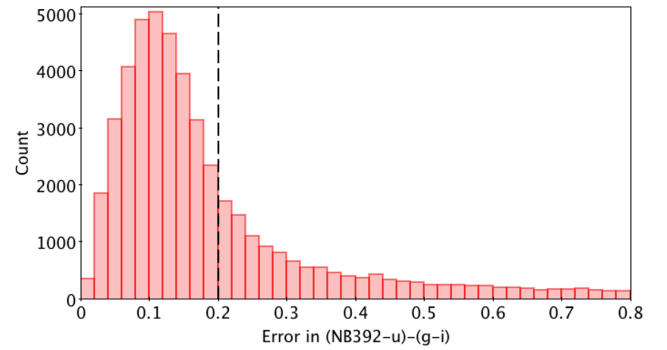


Figure 6. A histogram of the error in the magnitude difference $(\text{NB392}-u)-(g-i)$ for the whole catalogue. This error was limited to 0.2 so that sources with extreme values could be eliminated.

was plotted, shown in Figure 7. This is step 4 in Table 3. Using this, a limiting magnitude of 24.71 was found which is the peak after which the data is too faint to resolve and/or incomplete. After creating a subset including this reduction, a final reduced catalogue of 338 sources was found, a representation of which is shown in Figure 8.

3.2 Calculating the surveyable volume

One of the major goals of this investigation was to find the number densities of metal-poor stars within the galactic halo, so that they could be compared with the findings of other studies. As part of this, the volume of space surveyed needed to be calculated.

Calculating the area of sky that was surveyed was a vital part of the calculations. In order to find the area, the way the CCDs were overlaid against right ascension and declination was examined where the outlines of the CCDs can be seen in Figure 8. The value for area was found by taking the difference between the largest and smallest declination values, repeating this for the right ascension and then multiplying these values which gave an area of 1.89 deg². The large white spaces in Figure 8 are caused by the gaps between the CCDs themselves, and the masking of the data to account for internal noise of the CCDs. These gaps were not taken into consideration when calculating the area, meaning

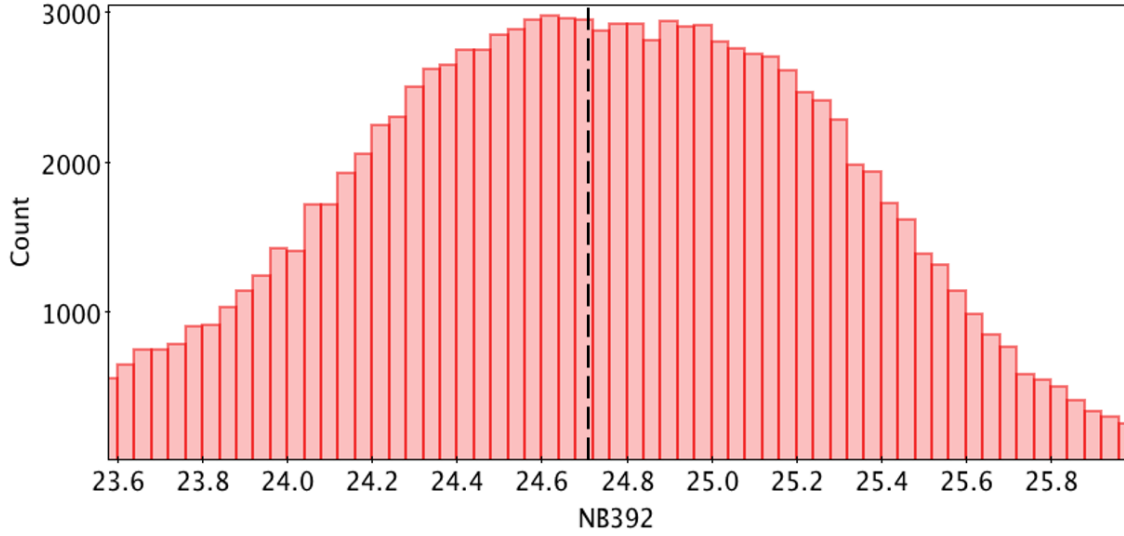


Figure 7. A histogram of NB392 magnitudes for the entire catalogue to find a limiting magnitude of 24.71.

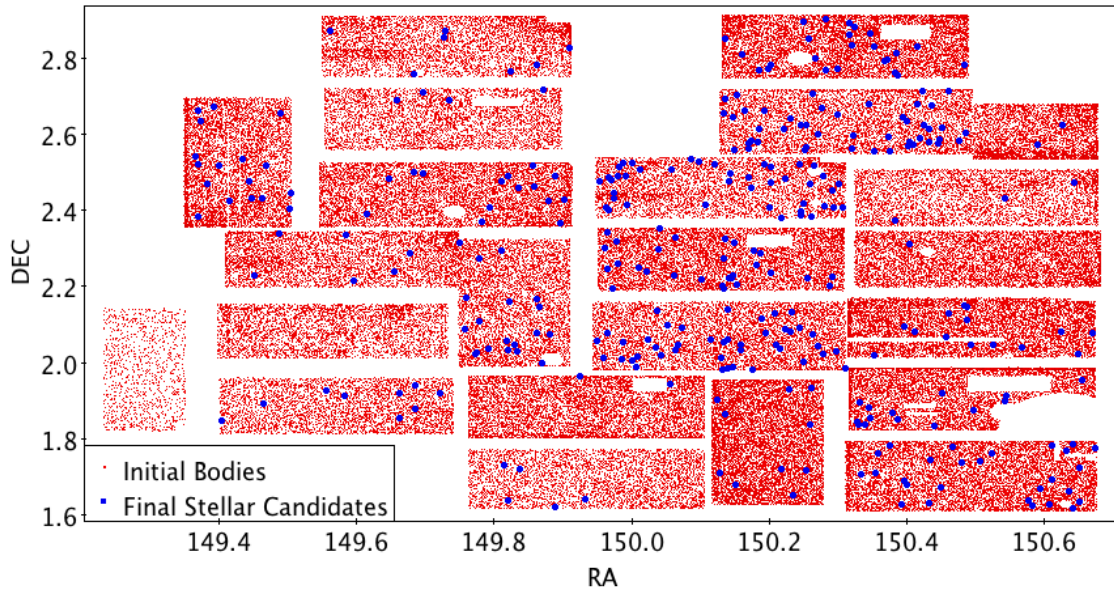


Figure 8. The on-sky positions, in degrees, of the 123,505 sources in the original NB392 catalogue overlaid with the 338 candidates for potential metal-poor stars where the steps taken to reduce the number of sources are summarised in Table 3. The white spaces within the quadrilaterals of sources are gaps in the catalogue created by masks used to eliminate areas contaminated by extremely bright sources. Any other white space is missing data not contained within the catalogue.

the value obtained is an upwards estimate of the true value. However, the error in the area will be ultimately negligible when other uncertainties in the calculations are taken into effect.

The area of sky which was surveyed in this investigation was 1.89 deg^2 , and the whole sky has a square area of $41,252.96 \text{ deg}^2$ (Guthrie 1947). The ratio of these two values is the area of sky that was surveyed as a fraction of the total sky, with a value of 4.58391×10^{-5} .

The different spectral classes of stars have different average luminosities and therefore different average absolute magnitudes. An M-type star is one of the coldest stars and so cannot be seen from anywhere near the distance that

the hottest O-type stars can be viewed from. Luminosity is proportional to temperature to the fourth power, with a hotter star having a more negative absolute magnitude than a colder star. The catalogue in this study will have been affected by this, with the maximum volume of space viewed differing by spectral class (Carroll & Ostlie 2018).

To perform these calculations, a limiting distance needed to be found for each spectral type which uses a limiting magnitude in the NB392 filter, m_l , found to be 24.71 in Section 3.1.4. An average magnitude per spectral type was also needed which was done using the theoretical data from the POLLUX database (Palacios, A. et al. 2010). The data was used to create multiple stars for each spectral type

Spectral class	Average M_{NB392}	Average volume (pc^3)
O	-4.69	8.55×10^{16}
B	-2.58	4.56×10^{15}
A	-0.348	2.18×10^{14}
F	0.981	4.66×10^{13}
G	3.89	1.47×10^{12}
K	7.73	6.68×10^{10}
M	10.1	1.89×10^8

Table 4. The various spectral classes along with their average absolute magnitude and their average surveyed volume which is an upper limit due to white spaces within the area surveyed not being taken into consideration. These values were calculated using a limiting magnitude in NB392 as well as generated stars using data from the POLLUX database.

which were then averaged to create a single star representative of that spectral type. Using Equation 5 and inserting a value of 24.71 for m_l and the theoretical values for absolute magnitude as M , the limiting distance per spectral type, D_l , was calculated.

$$D_l = 10^x \text{ where } x = \frac{m_l - M + 5}{5} \quad (5)$$

The volumes themselves could then be calculated using Equation 6, which uses the fraction of the total sky's surface area, $A_{\text{obs}}/A_{\text{sky}}$, to find the observed volume V_{obs} . The volumes that were calculated are shown in Table 4.

$$V_{\text{obs}} = \frac{4\pi D_l^3}{3} \frac{A_{\text{obs}}}{A_{\text{sky}}} \quad (6)$$

3.3 Classifying candidate stars

In order to obtain the spectral type of each of the candidate stars, the correlation between temperature and the value of the $g - i$ filter magnitude in theoretical data was used. Having created a graph of this, shown in Figure 9, a curve of best fit allowed an equation describing temperature in Kelvin with respect to $g - i$ to be produced, shown in Equation 7. Each source could then be classified into a spectral type, with the classifications by temperature shown in Table 2, and then applied to the catalogue.

$$T = 6800 - 2930(g - i) + 708(g - i)^2 + 203(g - i)^3 - 125(g - i)^4 + 15.4(g - i)^5 \quad (7)$$

3.4 Metallicity and its measurement

[Fe/H] is a logarithmic measure of a star's metal content as compared to that of the Sun. It is typically given as a difference of ratios of the metal in question's abundance, usually iron (in this case Ca, as discussed in Section 2), over hydrogen abundance between the observed star and the Sun (Matteucci 2001). The equation typically used for calculating metallicity is shown for iron, where N_{Fe} and N_{H} are the abundances of iron and hydrogen respectively.

$$[\text{Fe}/\text{H}] = \log_{10}\left(\frac{N_{\text{Fe}}}{N_{\text{H}}}\right)_* - \log_{10}\left(\frac{N_{\text{Fe}}}{N_{\text{H}}}\right)_{\odot} \quad (8)$$

The subtraction in Equation 8 means that the value given relates directly to the logarithmic difference in metal abundances, therefore a value of -1 would indicate that the star in question has one tenth the metallicity of the Sun while -2 would indicate a star of one hundredth the metal abundance of the Sun.

The method for determining the metallicities in this study took a more statistical approach, instead based on spectral information from the POLLUX database on 93 stars ranging from O to M-type. This method is discussed later in Section 3.6.

3.5 Predicting magnitudes

The POLLUX database is a source of synthetic spectral data created at the University of Montpellier in France (Palacios, A. et al. 2010). In order to obtain metallicity estimates, a catalogue of magnitudes for a range of theoretical stars of varying types and metallicities was first created for multiple filter profiles.

Using theoretical data obtained from the POLLUX database, values of flux density per unit wavelength ($\text{erg s}^{-1} \text{cm}^{-2} \text{\AA}^{-1}$) were obtained within the visual range of wavelengths (3000–12000 \AA) for stars ranging from M-types of temperature 3000K to O-types of temperature 49,000K. Profiles for the J , u , NB392, B , g , i , r , v , z and K filters were also provided. The profiles were normalised to ensure that the response in each filter had a range between 0 and 1 and the filter profiles were interpolated to the same wavelength values as the spectral data of each respective star for each use. The relevant flux density for each filter, the flux density that 'passed through' the filter, was then determined by convolving the normalised filter profile with the spectrum of each star.

The units throughout the magnitude calculation process needed to be consistent and were chosen due to their compatibility with both the AB magnitude equation, shown in Equation 9, and the provided wavelength units of the stellar spectra (\AA) and flux density per unit wavelength. The total flux density, which can be approximated to flux density per unit wavelength/frequency, in each case is then determined by integrating the filtered spectra flux densities over the range of wavelength values. The magnitude system decided upon was the AB magnitude system (Bessell 2005) which considers a source with a constant flux density per unit frequency. The equation for AB magnitude, M_{AB} , is shown below in Equation 9:

$$M_{\text{AB}} = -2.5 \log_{10} f_{\nu} - 48.60 \quad (9)$$

where $f_{\nu} = \frac{\lambda^2}{c} f_{\lambda}$

where f_{ν} is the flux density per unit frequency, f_{λ} is the flux density per unit wavelength, λ is the wavelength and c is the speed of light in a vacuum. The relation of f_{ν} and f_{λ} is necessary due to the fact that the derived flux density from the data is flux density per unit wavelength but the required flux density for use in the AB magnitude equation uses frequency. The -48.60 constant in the AB magnitude equation originates from the zero point of the system being about 3631 Janskys (Jy) where $1 \text{ Jy} = 10^{-26} \text{ WHz}^{-1} \text{ m}^{-2} = 10^{23} \text{ erg s}^{-1} \text{ Hz}^{-1} \text{ cm}^{-2}$.

Planck's radiation law (Derlet & Choy 1996) was used

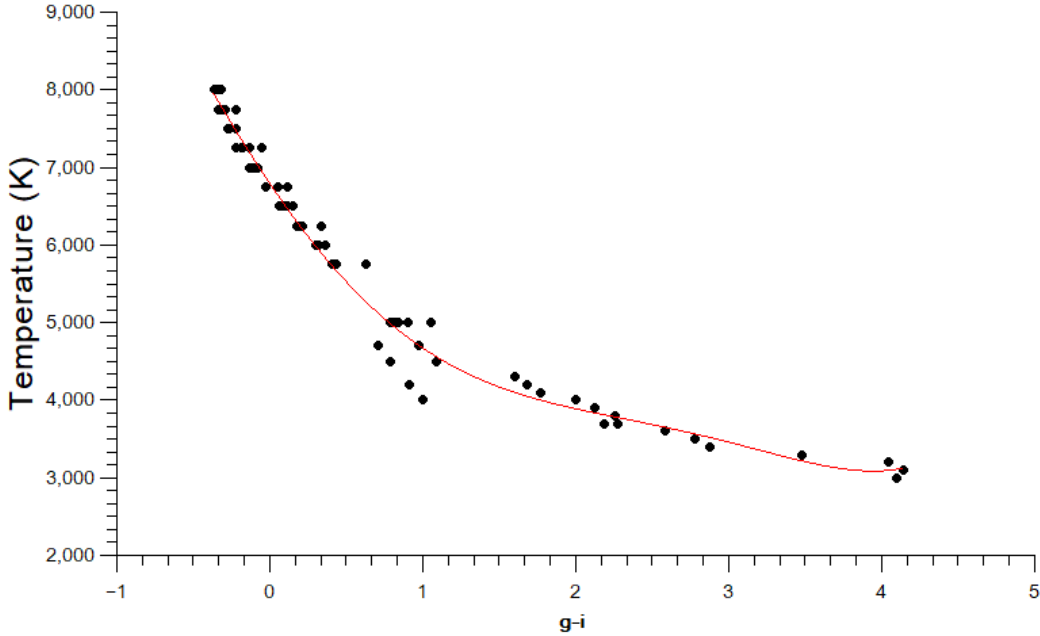


Figure 9. A graph showing correlation between $g-i$ and temperature which was used to obtain the curve of best fit where the equation is a fifth-order polynomial, shown as Equation 7. This equation was then used to calculate the temperature of the sources and obtain their spectral type using Table 2.

to theoretically extend the data into the infra-red. This is shown in Equation 10 where $B_\lambda(T)$ is the flux density, λ is the wavelength, T is the surface temperature of the star, h is Planck's constant, c is the speed of light in a vacuum and k_B is the Boltzmann constant.

$$B_\lambda(T) = \frac{2hc^2}{\lambda^5 (e^{\frac{hc}{\lambda k_B T}} - 1)} \quad (10)$$

Having extended the data, it now meant that a catalogue could be produced for a variety of stellar types and metallicities. A catalogue of colour index magnitude values in just the NB392, g , u and i filters was produced as it was decided after preliminary attempts at the creation of theory plots that a combination of these colour values provided the most apparent separation of metallicities. The chosen colour comparisons for the plot were $(\text{NB392}-u) - (g-i)$ and $g-i$, as this choice of colour axis produces an identifiable downward gradient (Melnyk et al. 2012). A plot of the chosen colour comparisons, with metallicity as a colour scale, was created to show the spread of metallicities with respect to their spectral types, shown in Figure 10.

In order to reaffirm the expected behaviour of $g-i$ values for stars of varying temperatures, and to ensure that the code was processing the filter and spectra correctly, a visual representation of g and i filters overlaid upon two stellar spectra was created, as shown in Figures 11 and 12. Any change in the peak of the spectra is due to the varying $g-i$ values for varying temperatures. As can be easily observed in stars of higher temperature, due to the shift towards the UV wavelengths of their peak compared to the spectra of a cooler star, one would expect the $g-i$ value of a star to decrease as a star's temperature increases. This is confirmed by observing this trend on Figure 9.

When the results were plotted over the observed data, the spread was far too small to make any real analy-

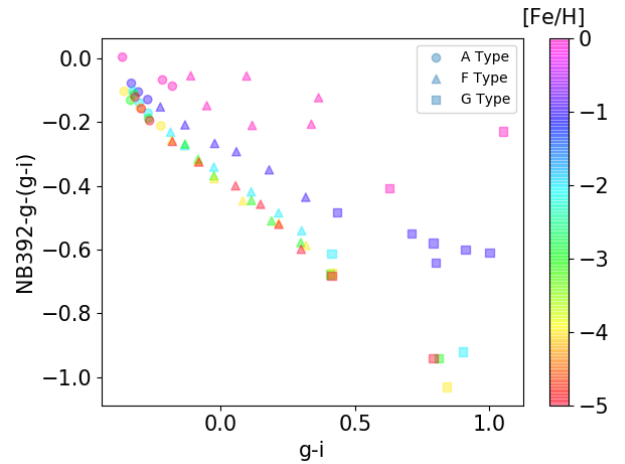


Figure 10. The initial colour-colour plot where there are noticeable layers of various metallicities with the variations in the layers decreasing with metallicity. The colour values for A, F, and G stars were the only ones plotted, as they were the only values available for all metallicities from 0 to -5.

sis, and the errors in the colour comparison values, discussed in Section 3.1.3, for each axis made any attempts to overlay this small set of data unfeasible. In order to make further distinctions and cuts within the observational data, a set of data with greater spread was required. An attempt to accomplish by merely modelling each point as a Gaussian distribution (Feller 1968) was made. Nevertheless, it was decided that using this method to create cuts was unscientific as the results and spread were not reproducible over multiple attempts. Instead, using the theoretical colour data, a

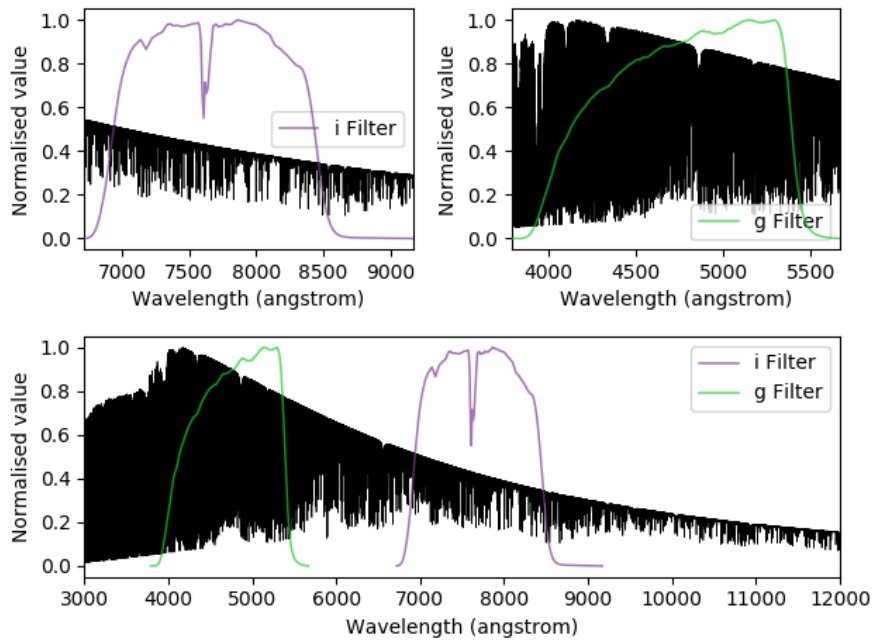


Figure 11. A plot of g and i filters on a zero metallicity F-type star of temperature 6,250K. The peak of the spectra can be seen to have shifted when compared to a hotter star (i.e. Figure 12); this peak shift is the cause of the change in $g - i$ values for stars of varying temperatures.

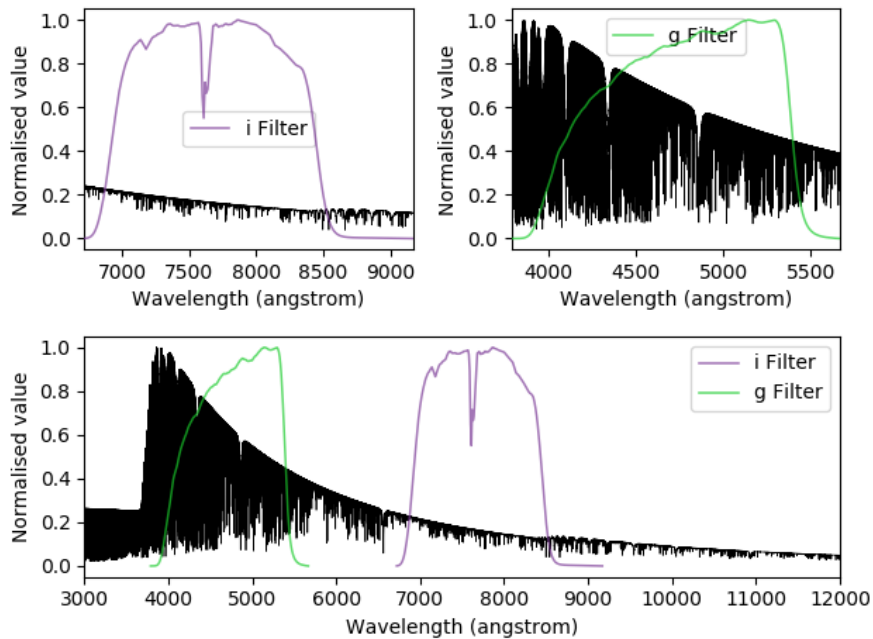


Figure 12. A plot of g and i filters on a zero metallicity A-type star of temperature 8,000K. The peak of the spectra can be seen to have shifted when compared to a cooler star (i.e. Figure 11); this peak shift is the cause of the change in $g - i$ values for stars of varying temperatures.

'heatmap' of multiple values for metallicity, was created with contour lines showing the boundaries for each increment in colour.

3.6 Creating a metallicity heatmap

The method described in Section 3.5 resulted in a collection of different theoretical stars at metallicities from 0 to -5 in a range of different filters. This allowed the generation of an x and y -axis of $g - i$ and $(NB392-u) - (g - i)$ respectively.

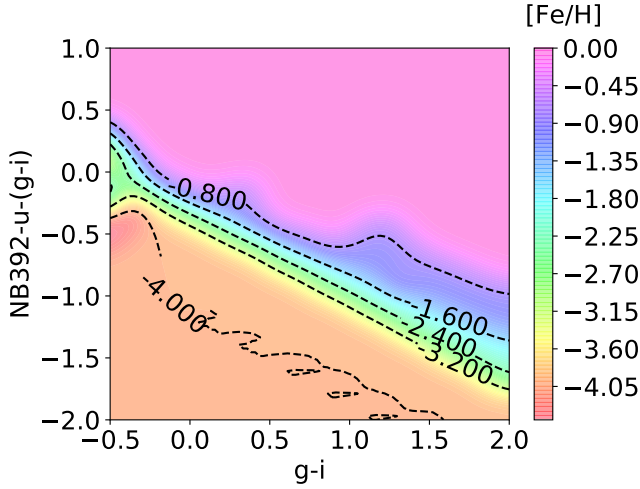


Figure 13. A heatmap to display $(\text{NB392}-u) - (g-i)$ against $g-i$ where the metallicities are displayed by the colour bar.

The y value uses $-(g-i)$ to make the lines flatter as they should not be dependent on the x value. These filters were chosen through a process of trial and error to get the broadest distinction between each of the metallicity lines as the larger the separation between lines, the easier it is to distinguish the different metallicities. The metallicity bands were almost linear, decreasing in x so the higher the metallicity, the higher the line on the graph. As such, the lower section of the plot would contain the most metal-poor stars.

There needed to be a way to automatically calculate metallicity for each star added, with errors. A visual extrapolation of the metallicity of a the star being analysed by it's position on figure 10 would be time consuming and would lack reproducibility. Since many of those points lie close together there would also be high errors in interpretation. The solution was to create a map of different regions of metallicities from the points in figure 10 and place stars to be determined on the plot. This would allow an automatic calculation of metallicity and the respective error. It also allowed for a large number of stars to be analysed and reproducibility. This heatmap is shown in figure 13 it was compiled in PYTHON using the following packages: SCIPY, ASTROPY, MATPLOTLIB and NUMPY.

Since there is a lack of data for the lower metallicities, below $[\text{Fe}/\text{H}]_{\text{NB392}} = -4$, any points in this region could have metallicities less than -4 but it cannot be determined here. Likewise, at the top of the plot, the 0 region has the same effect. However, since metal rich stars are of little interest to this investigation, it is not a cause for concern. The metal poor candidates would be analysed individually to more accurately determine their metallicity. Overall, the heatmap successfully allowed us to plot stars onto the colour-colour axis and determine a metallicity without the need for a visual inspection.

Details on the creation of this heatmap can be found in Appendix B.

3.6.1 Metallicity errors from photometric errors

The magnitudes from each filter, for every source, had an error. By taking this error, a Gaussian distribution could be created for each filter error. From this a value for the magnitude, in that filter, could be created with a variation using a value generated from the Gaussian of that filter's error. By doing this for all of the filters used in the calculation of x and y , a random point which followed the Gaussian distribution could be plotted. This was done 1000 times; then a median and a standard deviation were calculated. The median, which formed the metallicity associated with this point, was used over the mean as it is less affected by outliers and the standard deviation forms the error on this point. With this completed, metallicities for any star entered could be found.

3.7 Determining metallicities for candidate stars

In Figure 14, it is presented that many of the sources reside in the 0 to -1 $[\text{Fe}/\text{H}]_{\text{NB392}}$ region, as is commonly expected for most stars. The lowest values resided around the -4.0 region and any below that line had -4.0 with no variation or small error which is partly due to the lack of data below this point, as such the extrapolation just generated a region of -4.0 . This is also not a cause for concern as the heatmap was simply not able to determine metallicities less than -4.0 to any more accuracy. To measure anything less than -4.0 would require a direct measurement of the spectra which is a possible future step.

There are more stars in the -4.0 region than the -3.0 which is due to the larger size of the region. Although stars with $[\text{Fe}/\text{H}]_{\text{NB392}} < -4$ are rare, the uncertainty in the measurement of anything less than -4.0 results in a larger proportion in this bracket as they cannot be effectively separated.

Two of the 338 candidates did not fit in the boundaries set for the $[\text{Fe}/\text{H}]_{\text{NB392}}$ calculations so, since they went out of bounds, the candidates were excluded leaving 336 potential stars.

The error bars for the stars in this plot are not the same as the errors for $[\text{Fe}/\text{H}]_{\text{NB392}}$ (described in Section 3.6), however, since these are errors in the effective z -axis, there is no way to directly display the error in $[\text{Fe}/\text{H}]_{\text{NB392}}$. Instead, what is shown in Figure 14 is the average uncertainty in the colour-colour position for the set of stars being analysed here, calculated in Section 3.1.1.

3.8 Calculating number densities

Using the volumes for each of the spectral types found in Table 4 and the obtained number of stars per $[\text{Fe}/\text{H}]_{\text{NB392}}$ per spectral type, the number densities could be found. The candidates were split into groups of spectral type and $[\text{Fe}/\text{H}]_{\text{NB392}}$ and the number of candidates in each group were summed and divided by the surveyable volume for that spectral type which gave the number density per $[\text{Fe}/\text{H}]_{\text{NB392}}$ per spectral type. The errors in number density arise from a Poisson distribution on the number of stars in each bin of spectral type whereas the error in $g-i$ is the size (in $g-i$) for each spectral type.

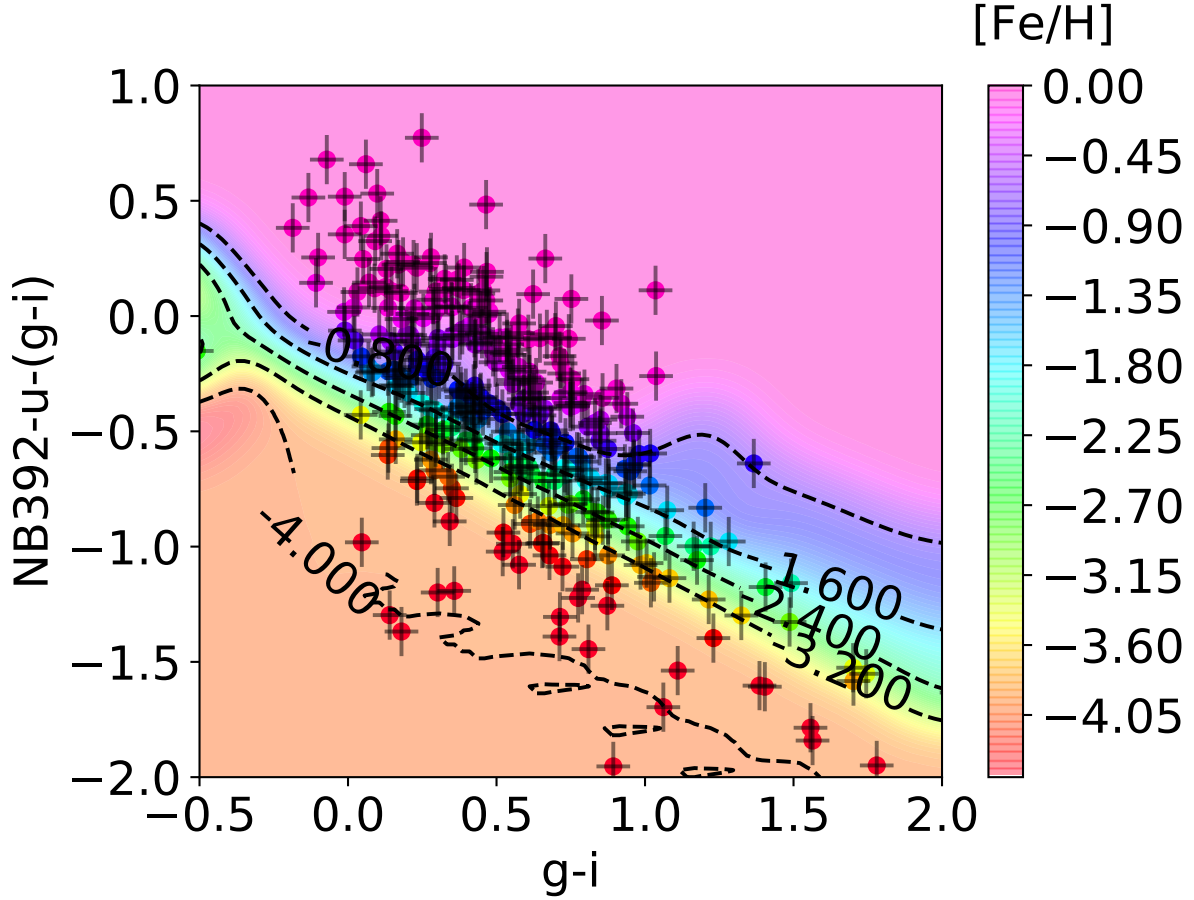


Figure 14. $(\text{NB392}-u) - (g-i)$ against $g-i$ where the metallicities are displayed by colour according to the colour bar. The points are the stars whose metallicities were to be calculated. There are 336 candidates which had $[\text{Fe}/\text{H}]_{\text{NB392}}$ calculated and displayed.

3.9 Visual inspection

After the stars were sorted into spectral type by $g-i$ value and had their metallicities calculated, each individual candidate was inspected. The table entries were given WARP designations in order of increasing metallicity before being individually inspected. It is worth noting that seven sources were classified as $[\text{Fe}/\text{H}] < -4$ due to the limitations of the heatmap discussed in Section 3.7 but may be lower.

WARP-1 to WARP-65 (the sources with perceived metallicities less than -3) were briefly examined by observing their right ascension and declination into the *HST* F814W COSMOS survey images and observing their visual profile on a compressed JPEG file. Sources with a particularly elliptical or smeared shape were labelled as galaxies whilst more point-like objects observed as potential stars had their raw ‘fits’ files examined more thoroughly in the SAOIMAGEDS9 astronomical imaging software. Examining the raw image in DS9 gave a greater degree of both detail and manipulation in the image, allowing for a more informed decision on the object to be made.

Once the cutout containing the source was displayed in the software, the image was altered to display in a ‘zscale’ format. This is a form of image processing within DS9 which automatically alters brightness and contrast for the image based on the minimum, maximum and median brightness

of an approximately 1,000 point sample. This makes the image more defined and potentially revealing previously unseen structure in the object. This was proceeded by a further increase in contrast to reveal any further minutiae. If the object, upon this more detailed inspection, was found to have a less point-like appearance than initially observed then it was, again, labelled as a galaxy.

4 RESULTS AND DISCUSSION

4.1 Final candidates

In order to only observe sources that may be metal-poor stars, the candidates being further investigated were limited to $[\text{Fe}/\text{H}]_{\text{NB392}} < -3$ putting them under the classification of extremely metal-poor (EMP); (Beers & Christlieb 2005). Upon further inspection, described in Section 3.9, seven metal-poor candidates were distinguishable where the image of each candidate is shown in Figure 15 and their details are shown in Table 5. These candidate stars have ID’s WARP-1, WARP-9, WARP-20, WARP-26, WARP-27, WARP-40 and WARP-57.

There were some uncertainties when distinguishing WARP-1 and WARP-9 due to some slight anomalous perturbations, and so further investigation may be required using

WARP-ID	Right Ascension (J2000)	Declination (J2000)	[Fe/H] _{NB392}	NB392 Magnitude
WARP-1	09:59:55.53	+02:30:48.64	-4.00 ± 0.03	24.534 ± 0.076
WARP-9	10:00:01.35	+01:59:15.81	-3.99 ± 0.01	24.025 ± 0.048
WARP-20	10:00:32.04	+02:11:40.13	-3.97 ± 0.08	24.287 ± 0.046
WARP-26	10:02:36.14	+01:38:03.23	-3.94 ± 0.14	24.315 ± 0.046
WARP-27	10:01:01.64	+02:51:11.42	-3.92 ± 0.17	24.338 ± 0.062
WARP-40	10:00:50.02	+02:07:43.83	-3.66 ± 0.32	24.221 ± 0.053
WARP-57	10:01:06.55	+02:29:26.66	-3.28 ± 0.43	24.339 ± 0.063

Table 5. The most likely metal-poor stars from 123,505 sources collected with the NB392 filter with their corresponding position, [Fe/H]_{NB392} and magnitude. Errors with a value smaller than 0.01 from the heatmap’s limitation were set to 0.01.

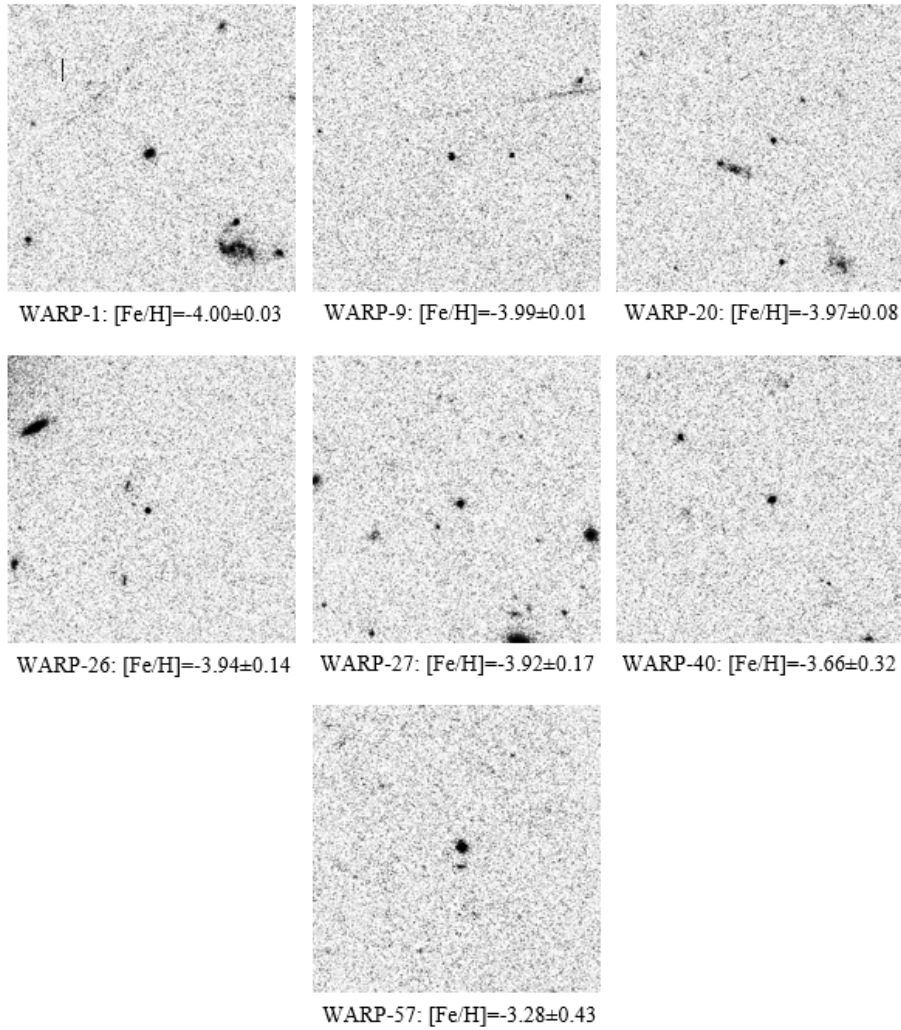


Figure 15. The final metal-poor star candidates showing their corresponding WARP-ID and estimated [Fe/H] value. The images were taken from NASA/IPAC Infrared Science Archive and have a size of $15'' \times 15''$.

higher resolution images of each source and studying each stellar spectra respectively to show any further structure and support this classification. The [Fe/H]_{NB392} values of WARP-9, WARP-20, WARP-26, WARP-27, WARP-40 and WARP-57 put these stars under the classification of EMP, whilst the value of WARP-1 puts it in the classification of ultra metal-poor (UMP) which is defined as $[\text{Fe}/\text{H}] < -4$ (Beers & Christlieb 2005). Other noteworthy sources also

include WARP-16, WARP-51 and WARP-52 due to complications when classifying or contamination from galaxies.

4.2 Number densities

The following sub-subsections state the obtained number densities per spectral type per metallicity band and compare these values, as well as metallicity distributions, with

expected values. $[\text{Fe}/\text{H}]_{\text{NB392}}$ lying between a range shall be discussed as the middle of that range, the exception being $0 \leq [\text{Fe}/\text{H}]_{\text{NB392}} < -0.5$, which shall be discussed as $[\text{Fe}/\text{H}]_{\text{NB392}} = 0$.

4.2.1 Number density values

The raw and revised number density values can be found in Table 6 and Figure 16. The reason for the low number density of A-type stars is due to there being only one A-type star in the data and their corresponding surveyed volume being orders of magnitude larger than others.

Overall the number densities from smallest to largest are type A, F, G and then K. This agrees with expectations as shown in Bovy (2017).

F and G-type stars have a large range of number densities for each metallicity. For both, their largest number density is at $[\text{Fe}/\text{H}]_{\text{NB392}}=0$ with volumes of $(9.2 \pm 1.4) \times 10^{-13} \text{ pc}^{-3}$ and $(4.51 \pm 0.98) \times 10^{-14} \text{ pc}^{-3}$ respectively. This is not surprising as the $[\text{Fe}/\text{H}]_{\text{NB392}}=0$ region is the largest in Figure 14 and the points are artificially set to be zero in this range. The most metal-poor value mapped, -4.0 , is not the smallest for all spectral types. This is probably due to the relative size of the region on Figure 14 that allows the classification in the -4.0 range. As discussed in Section 3.7, if there was more data to separate this region it would follow that this number density would decrease slightly. The higher galaxy contamination at lower metallicities would also increase this value. Also, one of the lowest number densities for F, G and K is -3 which is mostly due to the fact that the $[\text{Fe}/\text{H}]_{\text{NB392}} = -3$ range is the narrowest on the heatmap.

The number densities per $[\text{Fe}/\text{H}]_{\text{NB392}}$ in K are much closer together than those in F and G due to the fact there are fewer K candidates, hence the range of values for the number of stars will be smaller.

The contamination of 6.1% and the fact that galaxies will inherently display as metal-poor, means that statistically there is a larger chance of finding galaxies at a low $[\text{Fe}/\text{H}]_{\text{NB392}}$. Effectively removing galaxies from the data, as is discussed in Section 3.9, reduces the number density. On visual inspection of the images, 58 of the 65 candidates of $[\text{Fe}/\text{H}]_{\text{NB392}} < -3$ were galaxies.

4.2.2 Number densities compared to previous studies

After performing the visual removal of galaxies (see Section 3.9), the number densities were much lower than previously found, shown in Table 6. After summing all the number densities of the stars that fall within the criteria of EMPs and UMPs, this gives a total observed number density for both, shown in Table 7. In this case, $-2.5 \leq [\text{Fe}/\text{H}] < -3.5$ stars have been treated as satisfying the EMP criteria and $-3.5 \leq [\text{Fe}/\text{H}] < -4.5$ stars as satisfying the UMP criteria as the $[\text{Fe}/\text{H}]_{\text{NB392}}$ value of the stars cannot be determined to a more accurate extent. The expected number densities within this table are calculated in Appendix A.

When comparing the observed and expected values of number densities in Table 7, EMPs are in agreement with the data by a factor of ~ 10.8 and UMPs by a factor of ~ 6.3 with more UMPs but less EMPs observed than expected. These small discrepancies could be caused by numerous occurrences, such as the observed region of the halo being one

of particularly high UMP density, and it must be noted that the expected values are merely an estimation, and are subject to large uncertainties (Magg et al. 2019).

4.2.3 Metallicity distribution

From previous observations of the galactic halo, the metallicity of stars is expected to peak at $[\text{Fe}/\text{H}]_{\text{NB392}} \approx 1.8$ (Prantzos 2008) with a long tail to low metallicity stars according to data sourced from Norris et al. (1999) and Christlieb et al. (2004). A similar pattern to this is observed in this study, depicted in Figure 17, which uses the revised values of number density for $[\text{Fe}/\text{H}]_{\text{NB392}} < -3$. Another intuitive expectation for the $[\text{Fe}/\text{H}]_{\text{NB392}}$ distribution would be that the relative abundances decrease with $[\text{Fe}/\text{H}]_{\text{NB392}}$ values as it is widely accepted that metal-poor stars are more rare than those with higher metallicities.

The observed data correlates relatively well which can be observed in Figure 17 by similar characteristics to what was expected such as the long tail leading to lower $[\text{Fe}/\text{H}]_{\text{NB392}}$ values. Generally a higher abundance of K-type stars to G and F is observed, which is to be expected due to the lower lifetimes of G and F stars with respect to K-type stars. The obvious reason for the sudden drop in number density between $[\text{Fe}/\text{H}]_{\text{NB392}} \approx -3$ and $[\text{Fe}/\text{H}]_{\text{NB392}} \approx -2$ is that visual galaxy removal had only been performed on $[\text{Fe}/\text{H}]_{\text{NB392}} < -3$ stars, as these were the priority, and therefore any stars with metallicities larger than this could possibly be contaminated by galaxies. The small uplift in the number density at $[\text{Fe}/\text{H}]_{\text{NB392}} \approx -4$ is likely due to the approximation of the metallicity of stars at the lower boundary of the heatmap to be -4 , and thus this section of the plot is receiving more candidates than it would otherwise.

4.3 Comparison with LAMPSS (Worrell et al. 2019)

WARP has a sister project, LAMPSS, Lancaster Astrophysics Metal-Poor Star Search (see Worrell et al. 2019), who surveyed a similar area of sky to observe metal-poor stars, but used data collected with the MegaPrime/MegaCam on CFHT with the CaHK filter to observe calcium absorption in sources in the galactic halo.

By matching the reduced catalogues presented by both WARP and LAMPSS (Worrell et al. 2019), 42 matched sources were determined, however none of these are the candidates shown in Table 5 and Figure 15. For the full catalogue, the average metallicities were in good agreement with the values within this study. However, using the same limit of $[\text{Fe}/\text{H}]_{\text{NB392}} < -3$ the average metallicities were not in agreement, shown in Table 8. Although the WARP-64 has similar $[\text{Fe}/\text{H}]_{\text{NB392}}$ and $[\text{Fe}/\text{H}]_{\text{CaHK}}$, sources such as WARP-25 and WARP-37 have very different values.

The lack of overlap between the catalogues may be due to the initial separation of stars and galaxies from each data set. Differences in galaxy cuts may have excluded sources present in both catalogues, and any subsequent cuts within both catalogues excluding even more. The difference in metallicities could be due to the $[\text{Fe}/\text{H}]_{\text{CaHK}}$ values being integers and, taking into account that there are no errors, the LAMPSS values may take a wide range. If more precise values for $[\text{Fe}/\text{H}]_{\text{CaHK}}$ were calculated and errors were given, it

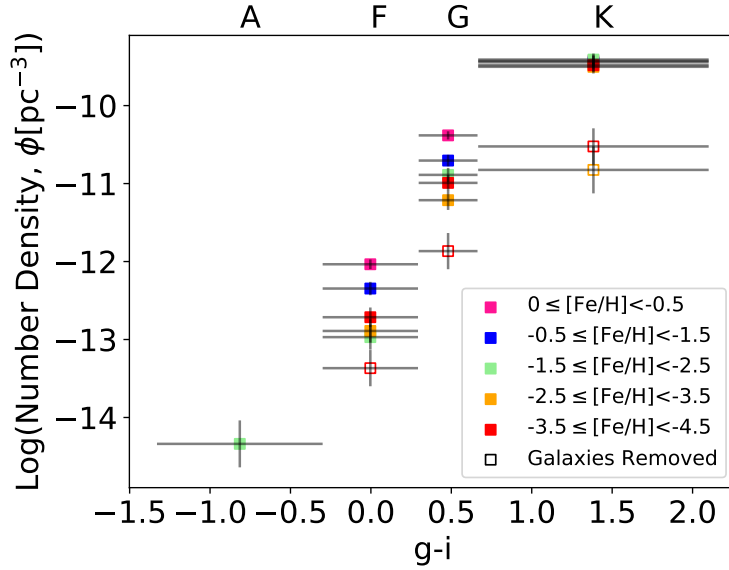


Figure 16. The number densities per spectral type per $[\text{Fe}/\text{H}]_{\text{NB392}}$ for all candidates in the halo of the Milky Way. The filled points are all of the candidates before visual inspection whereas the hollow points are after galaxies were removed by visual inspection of the candidates with $[\text{Fe}/\text{H}]_{\text{NB392}} < -3$ using the *HST* F814W high resolution images.

Spectral Type	$[\text{Fe}/\text{H}]_{\text{NB392}}$	Number Density (pc^{-3})	Number of sources in the catalogue
A	$0 \leq [\text{Fe}/\text{H}] < -0.5$	$< 4.6 \times 10^{-15}$	0
	$-0.5 \leq [\text{Fe}/\text{H}] < -1.5$	$< 4.6 \times 10^{-15}$	0
	$-1.5 \leq [\text{Fe}/\text{H}] < -2.5$	$(4.6 \pm 4.6) \times 10^{-15}$	1
	$-2.5 \leq [\text{Fe}/\text{H}] < -3.5$	$< 4.6 \times 10^{-15}$	0
	$-3.5 \leq [\text{Fe}/\text{H}] < -4.5$	$< 4.6 \times 10^{-15}$	0
F	$0 \leq [\text{Fe}/\text{H}] < -0.5$	$(9.2 \pm 1.4) \times 10^{-13}$	43
	$-0.5 \leq [\text{Fe}/\text{H}] < -1.5$	$(4.51 \pm 0.98) \times 10^{-13}$	21
	$-1.5 \leq [\text{Fe}/\text{H}] < -2.5$	$(1.07 \pm 0.48) \times 10^{-13}$	5
	$-2.5 \leq [\text{Fe}/\text{H}] < -3.5$	$(1.29 \pm 0.53) \times 10^{-13}$ [$< 2.1 \times 10^{-14}$]	6 [0]
	$-3.5 \leq [\text{Fe}/\text{H}] < -4.5$	$(1.93 \pm 0.64) \times 10^{-13}$ [$(4.3 \pm 3.0) \times 10^{-14}$]	9 [2]
G	$0 \leq [\text{Fe}/\text{H}] < -0.5$	$(4.15 \pm 0.53) \times 10^{-11}$	61
	$-0.5 \leq [\text{Fe}/\text{H}] < -1.5$	$(1.97 \pm 0.37) \times 10^{-11}$	29
	$-1.5 \leq [\text{Fe}/\text{H}] < -2.5$	$(1.29 \pm 0.29) \times 10^{-11}$	19
	$-2.5 \leq [\text{Fe}/\text{H}] < -3.5$	$(6.1 \pm 2.0) \times 10^{-12}$ [$< 6.8 \times 10^{-13}$]	9 [0]
	$-3.5 \leq [\text{Fe}/\text{H}] < -4.5$	$(1.02 \pm 0.26) \times 10^{-11}$ [$(1.36 \pm 0.96) \times 10^{-12}$]	15 [2]
K	$0 \leq [\text{Fe}/\text{H}] < -0.5$	$(3.74 \pm 0.75) \times 10^{-10}$	25
	$-0.5 \leq [\text{Fe}/\text{H}] < -1.5$	$(3.59 \pm 0.73) \times 10^{-10}$	24
	$-1.5 \leq [\text{Fe}/\text{H}] < -2.5$	$(3.89 \pm 0.76) \times 10^{-10}$	26
	$-2.5 \leq [\text{Fe}/\text{H}] < -3.5$	$(3.14 \pm 0.69) \times 10^{-10}$ [$(1.5 \pm 1.5) \times 10^{-11}$]	21 [1]
	$-3.5 \leq [\text{Fe}/\text{H}] < -4.5$	$(3.29 \pm 0.70) \times 10^{-10}$ [$(3.0 \pm 2.1) \times 10^{-11}$]	22 [2]

Table 6. The number densities and number of sources per spectral type per $[\text{Fe}/\text{H}]_{\text{NB392}}$. The square bracket numbers for the number of sources and number densities represent the revised values after the galaxies were removed by visual inspection of the sources with $[\text{Fe}/\text{H}]_{\text{NB392}} < -3$ using the *HST* F814W high resolution images.

would be possible to see how much the values of $[\text{Fe}/\text{H}]_{\text{CaHK}}$ and $[\text{Fe}/\text{H}]_{\text{NB392}}$ are actually in agreement. It was also provided that the lowest recorded metallicity LAMPSS star, LAMPSS_1229, has a metallicity $[\text{Fe}/\text{H}]_{\text{CaHK}} = -5$, but this may be speculative due to the lack of errors.

Another reason for the lack of matched sources may be due to differences in the magnitude limits and sky coverage. The area of sky observed by WARP was 1.89 deg^2 ,

while LAMPSS observed an area of 1.010 deg^2 (Worrell et al. 2019). This would therefore contribute to a lack of matched sources as the unmatched metal poor candidates may be outside the area surveyed by LAMPSS. There is also an offset in the two areas of sky shown in Figure WHATEVER, which would have contributed to the lack of overlap. It is a similar case for the maximum volume measured, as LAMPSS surveyed a maximum volume of $3.06 \times 10^{11} \text{ pc}^3$, and WARP

Metallicity Classification	Expected Number Density (pc^{-3})	Observed Number Density (pc^{-3})
EMP	4.96×10^{-10}	$(4.6 \pm 2.6) \times 10^{-11}$
UMP	4.96×10^{-12}	$(3.1 \pm 2.1) \times 10^{-11}$

Table 7. A comparison of the expected number density values for EMP and UMP found using an approximation of the size of the halo, the abundance EMPs and UMPs and the observed number densities after completing a visual galaxy removal.

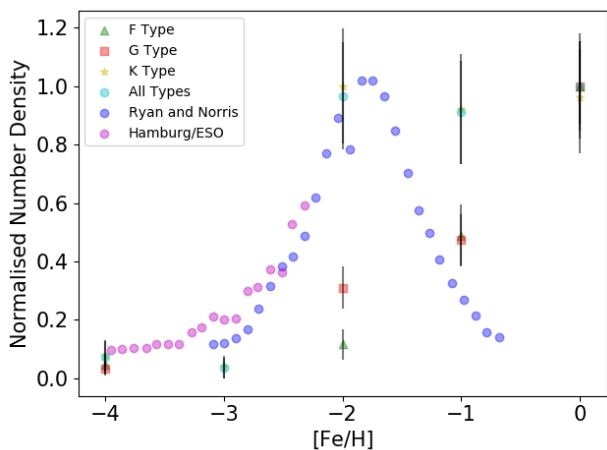


Figure 17. The observed (post-visual galaxy removal for $[\text{Fe}/\text{H}] < -3$ values) metallicity distribution for all stars within the observed area of Milky way halo as well as for F, G and K-type stars individually. Each stellar type has been normalised to its own greatest value. These results have been compared to previous studies performed by Norris et al. (1999) and the Hamburg/ESO Survey (Christlieb et al. 2004) which have also been normalised with respect to one another at $[\text{Fe}/\text{H}] \approx -2$. For a more detailed description, see Prantzos (2008).

surveyed a maximum volume of $8.55 \times 10^{16} \text{pc}^3$. This would not only affect the number of matched sources, as candidates presented by WARP may be outside the surveyed volume of LAMPSS, but would also explain the large number density values for each spectral type shown in Figure 18.

Figure 18 shows the number densities obtained in this study overlaid with the LAMPSS (Worrell et al. 2019) number densities for each spectral type. This plot shows that the number densities are not in agreement, with the LAMPSS values being much higher than the ones in this study. This is possibly due to the fact that LAMPSS may have been less strict with the cuts within their catalogue and therefore have a larger number of sources within a given volume in their final catalogue. They did not provide any cuts to discuss this further or any data that accounted for any galaxy contamination and so cannot be compared to the ‘galaxies removed’ values.

5 CONCLUSION

A catalogue of 123,505 sources (Sobral et al. 2017), selected via WFC with the NB392 filter using the Isaac Newton Telescope, was used to survey an area of 1.89 deg^2 with the

goal of finding metal-poor stars or their direct descendants as well as obtaining number densities for various metallicity values and spectral types. All metallicities given in this study were calculated from calcium abundance measured from the CaHK absorption lines due to these lines having a greater sensitivity to metal abundance than that of iron.

- A star-galaxy cut was made by inspection of sample star and galaxy groups obtained using spectroscopic redshift values of $z_{\text{spec}} = 0$ and $0.5 < z_{\text{spec}} < 7.0$ respectively. Based on these, a completeness of 75.3% and a contamination of 6.1% were calculated.

- Further cuts were made to the catalogue through limiting both errors and NB392 magnitude, shown in Figures 5, 6 and 7. The magnitude limit of 24.71 corresponded to a limiting distance and surveyed volume of 166 kpc and $1.47 \times 10^{12} \text{pc}^3$ respectively for G-type stars. The surveyed volumes for the remaining spectral types can be found in Table 4.

- After the remaining sources were overlaid onto a metallicity heatmap constructed from POLLUX data, 336 sources were assigned values of $[\text{Fe}/\text{H}]_{\text{NB392}}$. These were then sorted by $[\text{Fe}/\text{H}]_{\text{NB392}}$ and spectral type before being combined with the associated surveyed volumes for a number density of $(1.02 \pm 0.26) \times 10^{-12} \text{pc}^{-3}$ for sources classified as G-type with $-3.5 \leq [\text{Fe}/\text{H}]_{\text{NB392}} < -4.5$. A plot of number densities as well as a full results table are shown as Figure 16 and Table 6.

- The 65 sources with $[\text{Fe}/\text{H}]_{\text{NB392}} < -3$ were inspected using *HST* F814W high resolution images in DS9 imaging software to remove sources exhibiting galactic characteristics. After sources of this nature were removed, the number with $[\text{Fe}/\text{H}]_{\text{NB392}} < -3$ was reduced from 65 to seven.

- This study has found seven promising extremely metal-poor candidates in the halo of the Milky Way, shown in Table 5, with a possibility of them having an even lower metallicity due to limitations in the method used to determine their $[\text{Fe}/\text{H}]_{\text{NB392}}$. Most notable is that of WARP-1, the most metal-poor star in the study, with $[\text{Fe}/\text{H}]_{\text{NB392}} = -4.00 \pm 0.03$. Images of each of the seven stars are shown in Figure 15.

- Expected number densities of $4.96 \times 10^{-10} \text{pc}^{-3}$ and $4.96 \times 10^{-12} \text{pc}^{-3}$ were compared to the obtained number densities of $(4.6 \pm 2.6) \times 10^{-11} \text{pc}^{-3}$ and $(3.1 \pm 2.1) \times 10^{-11} \text{pc}^{-3}$ for EMP and UMP stars respectively. Where extremely metal-poor (EMP) are ($[\text{Fe}/\text{H}]_{\text{NB392}} < -3$) and ultra metal-poor (UMP) are ($[\text{Fe}/\text{H}]_{\text{NB392}} < -4$). The expected number densities were calculated using values estimated by Magg et al. (2019) and Bland-Hawthorn & Freeman (2000). This corresponds to an EMP number density approximately 10.8 times smaller than determined whilst the UMP number density is approximately 6.3 times larger than determined. While these differences may be as a result of a particularly UMP-rich and EMP-sparse region being observed, it is more likely to be as a result of the inherently large uncertainties in both the results and estimates (see Magg et al. 2019).

- The number densities of the sources formed a metallicity distribution which could be compared with the studies of Norris et al. (1999) and Christlieb et al. (2004) in Figure 17. When examining the metallicity distribution of all spectral types combined, the data points follow the distribution

WARP-ID	LAMPSS-ID	Right Ascension (J2000)	Declination (J2000)	$[\text{Fe}/\text{H}]_{\text{NB392}}$	$[\text{Fe}/\text{H}]_{\text{CaHK}}$
WARP-25	LAMPSS_1560	09:59:50	+02:00:46	-3.94 ± 0.10	0
WARP-37	LAMPSS_2	10:01:56	+02:36:15	-3.75 ± 0.36	-1
WARP-51	LAMPSS_767	10:00:03	+02:30:25	-3.39 ± 0.27	-2
WARP-63	LAMPSS_1669	09:59:05	+02:01:23	-3.05 ± 0.42	-2
WARP-64	LAMPSS_260	10:00:32	+02:41:34	-3.03 ± 0.39	-3

Table 8. All sources with $[\text{Fe}/\text{H}]_{\text{NB392}} < -3$ from the final WARP catalogue that have matched with LAMPSS sources (see [Worrell et al. 2019](#)), showing their positions, WARP-ID and corresponding LAMPSS-ID, $[\text{Fe}/\text{H}]_{\text{NB392}}$ calculated by WARP and $[\text{Fe}/\text{H}]_{\text{CaHK}}$ calculated by LAMPSS. It can be seen that there are large discrepancies between the metallicity values, especially WARP-25 which has $[\text{Fe}/\text{H}]_{\text{NB392}} \approx -4$ but also $[\text{Fe}/\text{H}]_{\text{CaHK}} = 0$.

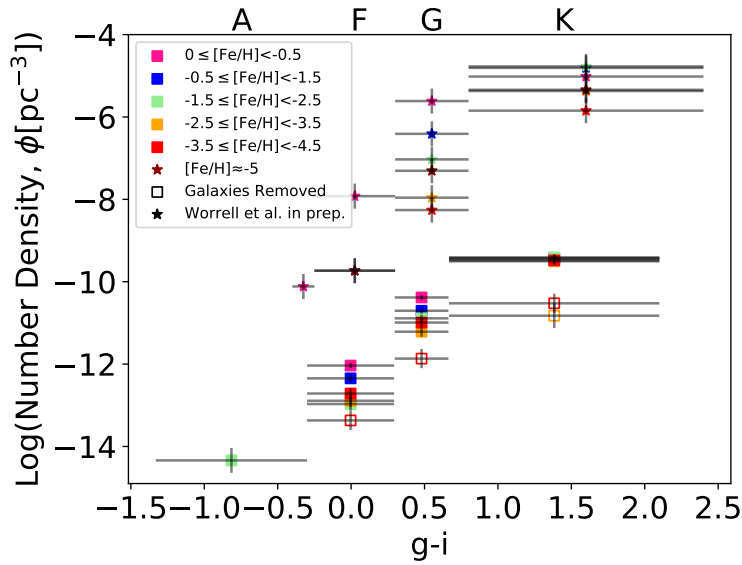


Figure 18. The number densities per spectral type per $[\text{Fe}/\text{H}]_{\text{NB392}}$ for all sources in the halo of the Milky Way. The filled squares are all of the candidates before visual inspection whereas the hollow squares are after galaxies were removed by visual inspection of the sources with $[\text{Fe}/\text{H}]_{\text{NB392}} < -3$. The stars are the number densities obtained by WARP’s sister project, LAMPSS (see [Worrell et al. 2019](#)).

quite closely for $[\text{Fe}/\text{H}]_{\text{NB392}} \leq -2$ which is the region of interest to this study. This distribution agreement supports the $[\text{Fe}/\text{H}]_{\text{NB392}}$ values assigned to the candidates for this region.

- When results were compared with the LAMPSS study ([Worrell et al. 2019](#)) who used the MegaPrime/MegaCam equipped with the CaHK filter at CFHT to measure calcium abundance, unfortunately none of the sources found in Table 5 could be matched to their results. Overall for the sources with $[\text{Fe}/\text{H}] < -3$ which could be matched, there is very little corroboration between the data, as shown in Table 8. In the case of WARP-25 (LAMPSS_1560), the results of $[\text{Fe}/\text{H}]_{\text{NB392}} = -3.94 \pm 0.10$ and $[\text{Fe}/\text{H}]_{\text{CaHK}} = 0$ are very much in disagreement. It is hard to determine where this large discrepancy originates but the limitation of the LAMPSS data to integer values as well as a complete lack of errors makes anything beyond direct comparison highly speculative and, given the agreement of the metallicity distribution, it is within reason to assume that the $[\text{Fe}/\text{H}]_{\text{CaHK}}$ values are more likely to be at fault.

6 FUTURE WORK

Oversight led to the figures and results given in this study not being adjusted to account for the 75.3% completeness of the catalogue after cutting. The various number densities and distributions could, in future, be adjusted to account for the 24.7% of objects not included in the catalogue.

Seven candidates were found for extremely metal-poor stars with $[\text{Fe}/\text{H}]_{\text{NB392}} < -3$ but spectroscopic observations are required in order to confirm these findings. The absorption spectra of these stars can be also be analysed to find their $[\text{Fe}/\text{H}]$ values. The seven candidates all have an NB392 magnitude of greater than 24, as shown in Table 5, so they are incredibly faint. Spectroscopic analysis of these candidates would only be possible with a large telescope, therefore a proposal to the ESO has been submitted to direct the VLT to look at them.

This investigation into the number densities of metal-poor stars in the halo of the Milky Way is over a relatively small area of sky ($\sim 1.9 \text{ deg}^2$). There have been a range of sky surveys intending to locate metal-poor stars in the halo such as the Pristine survey ([Caffau et al. 2017](#)), the

HK and Hamburg/ESO (HES) surveys (Beers et al. 1990; Christlieb et al. 2002) and the SkyMapper Survey (Keller et al. 2012) which surveyed areas of over 1,000, 7,000 and 20,000 deg² respectively. By increasing the region of sky examined to a significant fraction of these surveys, WARP’s [Fe/H]_{NB392} distributions would be more representative and could be compared more directly to those of the other surveys. In Table 7, the number density of EMP stars that was found was ~ 10.8 times smaller than the expected values in Magg et al. (2019), but the number density of UMP stars that were detected was ~ 6.3 times greater than expected. Another reason for increasing the total area of observation is that these number densities could be recalculated and compared with the expected values to see if they correspond accordingly or whether the area of sky surveyed has different component amounts of metal-poor stars to other areas of sky.

One of the biggest issues faced was the inability to accurately classify stars with [Fe/H]_{NB392} < -4 which was partially due to the fact that at lower [Fe/H]_{NB392} values the colour differences separating them became less distinct, as depicted in Figure 10. The likely cause of this lack of distinction is due to the fact that the effect of the CaHK absorption is decreased at lower [Fe/H]_{NB392} values when compared to higher ones. This absorption effect is illustrated in Figure 2. Our method of assigning [Fe/H] values (see Section 3.7) can contaminate the higher [Fe/H]_{NB392} values by averaging them with the lower ones. This may mean that the current number density for [Fe/H]_{NB392} = -4 stars may be artificially inflated due to the inability to assign lower values. By having even lower values such as [Fe/H]_{NB392} < -5, the relative colours of more metal-poor stars can be more accurately predicted and the number densities improved. This would be implemented by adding a series of theoretical black body stars into the [Fe/H]_{NB392} assigning code.

ACKNOWLEDGEMENTS

The authors would like to thank Tom Cornish for making available their original metallicity heatmap PYTHON code. The thorough comments and simple structure allowed us to grasp the concepts required for forming the basis of the heatmap used in this work. We are grateful to the work of Tania Machado and Alice Pygott and to the many fruitful discussions with the LAMPSS collaboration. We would also like to thank David Sobral for the continuing support during the project, and also for the useful information from various lecture courses. We have benefited immensely from the publicly available programming language PYTHON, including NUMPY (Oliphant 2006), SCIPY (Jones et al. 2001), MATPLOTLIB (Hunter 2007) and ASTROPY (Astropy Collaboration et al. 2018) as well as the TOPCAT analysis program (Taylor 2005) and the SAOIMAGEDS9 astronomical imaging software (Joye & Mandel 2003).

REFERENCES

Astropy Collaboration et al., 2018, *AJ*, **156**, 123
 Beers T. C., Christlieb N., 2005, *ARA&A*, **43**, 531
 Beers T. C., Preston G. W., Shectman S. A., Kage J. A., 1990, *AJ*, **100**, 849

Bell E. F., et al., 2008, *ApJ*, **680**, 295
 Bessell M. S., 2005, *ARA&A*, **43**, 293
 Bland-Hawthorn J., Freeman K., 2000, *Science*, **287**, 79
 Bovy J., 2017, *MNRAS*, **470**, 1360
 Caffau E., et al., 2017, *Astronomische Nachrichten*, **338**, 686
 Carroll B. W., Ostlie D. A., 2018, An introduction to modern astrophysics. Cambridge University Press
 Chon S., Latif M. A., 2017, *MNRAS*, **467**, 4293
 Christlieb N., Wisotzki L., Graßhoff G., 2002, *A&A*, **391**
 Christlieb N., Reimers D., Wisotzki L., 2004, *The Messenger*, **117**, 40
 Derlet P. M., Choy T. C., 1996, *Aust. J. Phys.*, **49**, 589
 Feller W., 1968, An Introduction to Probability Theory and its Applications Vol. I. Wiley
 Gray R. O., Corbally C. J., 2009, *Stellar Spectral Classification*. Princeton University Press
 Guthrie D. V., 1947, *Popular Astronomy*, **55**, 200
 Hosokawa T., Hirano S., Kuiper R., Yorke H. W., Omukai K., Yoshida N., 2016, *ApJ*, **824**, 119
 Hunter J. D., 2007, *Computing In Science & Engineering*, **9**, 90
 Johnson H. L., Morgan W. W., 1953, *ApJ*, **117**, 313
 Jones E., Oliphant T., Peterson P., et al., 2001, SciPy: Open source scientific tools for Python. <http://www.scipy.org/>
 Joye W. A., Mandel E., 2003, in Payne H. E., Jędrzejewski R. I., Hook R. N., eds, *Astronomical Society of the Pacific Conference Series Vol. 295, Astronomical Data Analysis Software and Systems XII*. p. 489
 Keller S. C., Skymapper Team Aegis Team 2012, **458**, 409
 Keller S. C., et al., 2014, *Nature*, **506**, 463 EP
 Lee A. T., Stacy A., Bromm V., 2016, *MNRAS*, **462**, 1307
 Magg M., Klessen R. S., Glover S. C. O., Li H., 2019, *MNRAS*,
 Matteucci F., 2001, *The Chemical Evolution of the Galaxy*. Astrophysics and Space Science Library, Springer Netherlands, <https://books.google.co.uk/books?id=PT701nS7CksC>
 Melnyk O. V., Dobrycheva D. V., Vavilova I. B., 2012, *Astrophysics*, **55**, 293
 Norris J. E., Ryan S. G., Beers T. C., 1999, *ApJS*, **123**, 639
 Oliphant T., 2006, *NumPy: A guide to NumPy*, USA: Trelgol Publishing, <http://www.numpy.org/>
 Palacios, A. Gebran, M. Josselin, E. Martins, F. Plez, B. Belmas, M. Lèbre, A. 2010, *A&A*, **516**, A13
 Prantzos N., 2008, *A&A*, **489**, 525
 Scoville N., et al., 2007,] 10.1086/516585, **172**, 1
 Sobral D., Matthee J., Darvish B., Schaerer D., Mobasher B., Röttgering H. J. A., Santos S., Hemmati S., 2015, *ApJ*, **808**, 139
 Sobral D., et al., 2017, *MNRAS*, **466**, 1242
 Starkenburg E., et al., 2018, *MNRAS*, **481**, 3838
 Stroe A., Sobral D., 2015, *MNRAS*, **453**, 242
 Stroe A., Sobral D., Röttgering H., van Weeren R., 2014, *MNRAS*, **438**, 1377
 Taylor M. B., 2005, in Shopbell P., Britton M., Ebert R., eds, *Astronomical Society of the Pacific Conference Series Vol. 347, Astronomical Data Analysis Software and Systems XIV*. p. 29
 Worrell E., Patel N., Wresilo K., Dicker S., Bray O., Bagness J., Sobral D., 2019, *NLUAstro*, **1**, 75
 Youakim K., et al., 2017, *MNRAS*, **472**, 2963
 Zhu G., Ménard B., 2013, *ApJ*, **773**, 16

APPENDIX A: EXPECTED NUMBER DENSITIES

This section contains a short overview of the method to obtain N_{EMP} and N_{UMP} (Magg et al. 2019), the number of EMP stars and UMP stars in the halo respectively, as well

as the method for calculating their expected number densities.

From previous studies (Bell et al. 2008), the halo can be estimated to be of mass $M_{\text{halo}} \approx 10^9 M_{\odot}$. Using this, the estimations that 1/800 stars in the halo are EMP and 1/80,000 are UMP (Youakim et al. 2017), and an approximation that the average star mass is $M_{*} \approx 0.6 M_{\odot}$, estimations of the numbers of EMPs and UMPs in the halo can be found, shown in Equations A1 and A2.

$$N_{\text{EMP}} = \frac{M_{\text{halo}}}{800M_{*}} \approx 2.08 \times 10^6 \quad (\text{A1})$$

$$N_{\text{UMP}} = \frac{M_{\text{halo}}}{80,000M_{*}} \approx 2.08 \times 10^4 \quad (\text{A2})$$

By making the assumption that the halo is spherical and of the size $R_{\text{halo}} \approx 100\text{kpc}$ (Bland-Hawthorn & Freeman 2000), an approximation of the volume of the halo can be made of $V_{\text{halo}} \approx 4.19 \times 10^6 \text{ pc}^3$ using the equation of the volume of a sphere. Thus, estimations of the number densities of EMPs and UMPs in the galactic halo are found using equation A3.

$$n_{i,\text{expected}} = \frac{N_i}{V_{\text{halo}}} \quad (\text{A3})$$

APPENDIX B: CREATING THE HEATMAP

The first task was to group the data into different metallicities such that each metallicity had its own x and y array. This then allowed the creation of a 1D interpolation for each metallicity which was done to ensure that any x value could find its corresponding y value.

To make a heat map, a grid was created. Firstly, the range of the grid was specified, with the maximum and minimum points being stored such that they could be used for a later calculation. For each metallicity, a large series of points were generated for x , using the max and min set by the maximum and minimum for each set of metallicity points. Then using the interpolation from earlier, a corresponding series of y points are found and the metallicities are assigned as an array of constant values in the z -axis.

Finally, these three axes were brought together which created a 3D grid of data points, each with a metallicity associated. The grid was bound using the maximum and minimum points stored earlier and since there are 100 points between the maximum and minimum, a 100x100 grid was created. The z values were smoothed using a Gaussian to ensure that there are better transitions between each of the metallicity sections. This then allowed a metallicity heatmap plot to be created with the contour lines being calculated by PYTHON.

To increase the range of $g - i$ values that could be used to calculate metallicities, the data points from the theoretical data were extended using polyfit polynomials. Using masks for the metallicity types, each metallicity had its own 1D interpolation using a polynomial to extrapolate the data but there were issues regarding the order of the polynomial. There are few data points, as such, any slight curvature would cause a large extrapolation either up or down. This, in turn, resulted in contamination of the heatmap above the zero metallicity line, which should be constant. To reduce

this, the polynomials were made to be first order and the data was artificially enhanced above the zero line to ensure all of those points remained at zero metallicity. These artificial points would not reduce the certainty in the data as it is a reasonable assumption that all stars above the zero metallicity line would only have zero metallicities. This was deemed justifiable as they are not the points of interest. Figure 13 shows the final heatmap.

Next, the metallicities for any inputted star had to be calculated. The first issue was the blank spaces left by magnitudes not calculated. When PYTHON tried to access the blank spaces it would crash, the solution was to use a mask that only allowed values greater than 0 to be used.

To find $[\text{Fe}/\text{H}]_{\text{NB392}}$ for the sources, the points had to be mapped to the grid which formed the heatmap, as explained in Section 3.6. Even though the range was specified using $g - i$ values, a grid with 100 points was used on the x and y -axis which have metallicities assigned. As such, requesting a z value for a point that does not exist on the grid would return an error. The point would have to be mapped to the x and y -axis using a simple linear equation, shown in Equation B1, where GridValue is the integer value on the 100x100 grid, $value$ is the inputted value, a_{max} is the maximum value and a_{min} is the minimum value on the axis in Figure 13.

$$\text{GridValue} = \left(\frac{99}{a_{\text{max}} - a_{\text{min}}} \right) * (value - a_{\text{min}}) \quad (\text{B1})$$

APPENDIX C: FURTHER DETAIL ON ABSOLUTE FLUX

In order to find the relevant flux densities for each filter, the respective product of the response in the filter and flux density of the spectral data was found. Since the units of the provided flux densities were uncertain (merely described as ‘absolute flux’), a scaling factor between cgs units and the determined flux was needed. This was accomplished by obtaining, using the POLLUX database, a spectrum of a star of known luminosity ($L_{\text{cal}} = 5.918588 \times 10^{34} \text{ erg s}^{-1}$) and finding the ratio of the code’s luminosity output based on POLLUX data and its actual luminosity in cgs units. This ratio can be used to multiply the flux and produce correct magnitudes.

There were problems obtaining magnitude values as the code initially produced obviously unphysical and unreasonable magnitude values of approximately -80 . The problem was determined to be that the POLLUX database ‘absolute flux’ units had been interpreted to be the values at 10pc as desired - the use of ‘absolute’ implied as much. However, this was not the case, hence why the ratio factor was introduced into the calculation of magnitude.

This paper has been typeset from a $\text{T}_{\text{E}}\text{X}/\text{L}^{\text{A}}\text{T}_{\text{E}}\text{X}$ file prepared by the author.